Chapter 7 -- Heating Methods

NCSX has been designed to accommodate a variety of heating systems, including ohmic heating, neutral beam injection, and two different strategies for ICRF. The plan is to initially provide ohmic heating and 3MW of balanced neutral beam injection for initial experiments. Subsequent upgrades could add an additional 6 MW of ICRF and 3 MW of neutral beam injection.

7.1 Ohmic Heating

The ohmic heating capability is implemented using the poloidal field coils, and provides inductive heating from up to 420 kA of ohmic current. This will be used for initial breakdown and formation of target plasma for neutral beam heating. It will also be used to manipulate the current profile shape, allowing relatively rapid equilibration with the bootstrap current, as discussed in Chapter 9.

7.2 Neutral Beam Injection Heating

7.2.1 Neutral Beam System Characteristics

7.2.1.1 Available Injection Power

NCSX will use the present PBX-M NBI system, consisting of 4 beamlines. The ion sources have 30 cm circular copper grids and a focal length of 440 cm. Each ion source was fabricated, tested, and fully qualified at ORNL in 1979-1980 to power levels of 1.5 MW, H^0 (@ 50 KV, 100A, 0.3 sec). In addition at ORNL, one ion source was demonstrated to yield 2 MW, D^0 (@ 50 KV, 70A, 0.3 sec). The injected power for a given species is proportional to the injection energy to the 5/2 power. Subsequent testing after installation on PDX demonstrated the capability to inject with four sources 8.3 MW D^0 in the absence of magnetic fields. The presence of stray magnetic fields and finite transition duct pressure reduced the available power to 6.5-7.0 MW D^0. This loss of reionization power of 12-18% will be regained by reinstalling the 100 kl/s cryopumping capability of the original design.

7.2.1.2 Pulse Length

The neutral beamline power handling surfaces are engineered to operate at a maximum of 500 msec pulse lengths at the full power peak power density of 3 kW/cm^2. In addition to power conditioning each of the ion sources at pulse lengths of 300 msec, ORNL in 1979-1980 demonstrated one ion source to operate at 500 msec pulse lengths using H^0 at about 50 KV, 90A. Similar results were obtained on PBX-M, where each of the 4 neutral beamlines was demonstrated to operate with D^0 at ~40 KV, 1 MW , to pulse lengths of 500 msec. Operation to higher powers at 500 msec seemed feasible for both H^0 and D^0 and should be considered available for NCSX. In addition, the MAST experiment, which is presently using similar ORNL style beamlines is planning to upgrade to 1.5-3 second pulse length capability. If this is successful, NCSX will be able to adopt this technology for long pulse NBI.

7.2.1.3 Control and Performance

After NBI installation, PPPL developed full computerization for the NBI system, including control of filament, arc, and accel conditioning, and fault response using an "artificial intelligence" or "expert rules" algorithm. One operator monitors all four systems in a “hands-off” manner. The computer control provided unforeseen benefits in operational reliability, reproducibility, and safety.

7.2.1.4 Ion Source Focal Length, Focusing, and Power Density Profiles

The PBX-M ion sources consist of 3 circular grids, 30 cm in diameter containing about 2000 circular holes for producing 2000 circular beamlets. The grids are shaped spherically concave to provide geometric focusing (aiming) with a focal length of 440 cm, which was the distance to the PDX torus port (Figure 7-1).

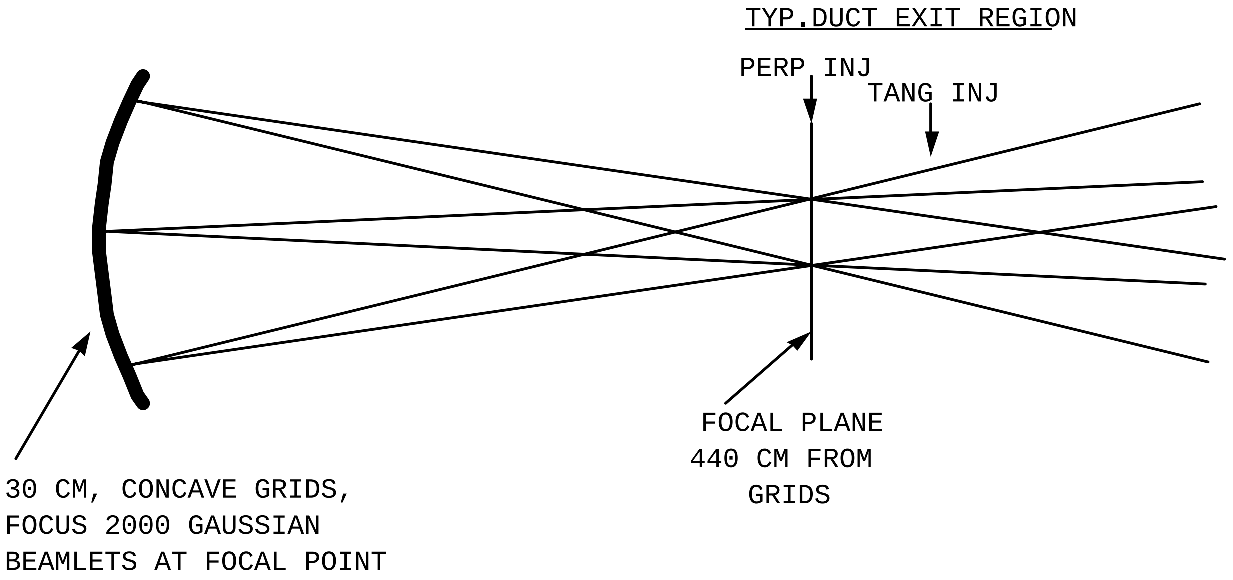

Figure 7-1. Schematic diagram of PBX-M ion source grid optics. The ion source grids are curved so as to focus 2000 Gaussian beamlets at a focal point 440 cm from the grids. Ion source optics determine the duct size and achievable aiming angles

The required grid curvature was modeled by J. Whealton (ORNL) using a Gaussian geometric optics code. Measurements of the respective as-built focal lengths and focusing were performed using a pinhole camera technique and power density profile measurements at the focal plane torus target. The final measured focal lengths were consistent with the design value of 440 cm. Table 7-1 gives the H^o angular divergences for each neutral beam at the torus target horizontal focal plane (440 cm). The results shown in Table 7-1 were obtained from measurements of the respective beam power density profiles measured along the horizontal axis in the focal plane at the torus target using a scanning water calorimeter behind pin-hole apertures (Figure 7-2). The semi-log plots exhibit Gaussian behavior down to about 10% of full power. Below the 10% power level, the profiles exhibit "wings" that have been characterized by asymmetric Gaussian, or polynomial least-squares fitting.

NBI System [a)]	$\theta_{HW@HM}$ [b)]	$W_{HW@HM}$ [c)]	$\theta_{HW@1/e}$ [d)]	$W_{HW@1/e}$ [e)]
S	1.5°	11.58 cm	1.8°	13.9 cm
E	1.13°	8.75 cm	1.36°	10.5 cm
NW	1.2°	9.25 cm	1.44°	11.1 cm
SW	0.94°	7.25 cm	1.13°	8.7 cm

Table 7-1. Summary of NBI optics.

Notes

[a)] **NBI System listed in order of ion source fabrication and testing at ORNL.**
[b)] **Angular divergence from centerline to edge at one-half of full power.**
[c)] **Angular divergence from centerline to edge at 1/e of full power.**
[d)] **Beam half-width from centerline to edge at one-half of full power.**
[e)] **Beam half-width from centerline to edge at 1/e of full power.**

NCSX NBI access requirements depend on the desired injected power, which in turn depends on the effective focal length, focusing, and steering of the output neutral beam. These factors are essentially significant considerations in the design of long, tight, transition ducts for tangentially injecting beams. Preliminary NCSX neutral beam configurations and transition duct designs use the above results.

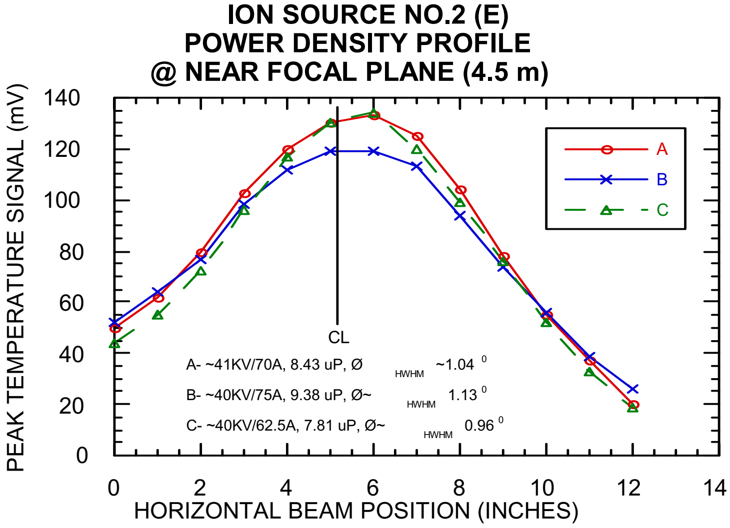

Figure 7-2. Power density profile measured at ORNL for PDX ion source No.2 (East NBI). Note that the resultant beam trajectory at the torus target at the exit of the transition duct is not entirely determined by simple, *apriori* mechanical alignment of the ion source. Measuring the actual bean position in the duct is important for proper beam alignment

The solid and dashed lines in Figure 7-3 show the simulated beam power density profile along the beam axis using the J. Whealton (ORNL) gaussian geometric optics code fit to the measurements given in Table 7-1.

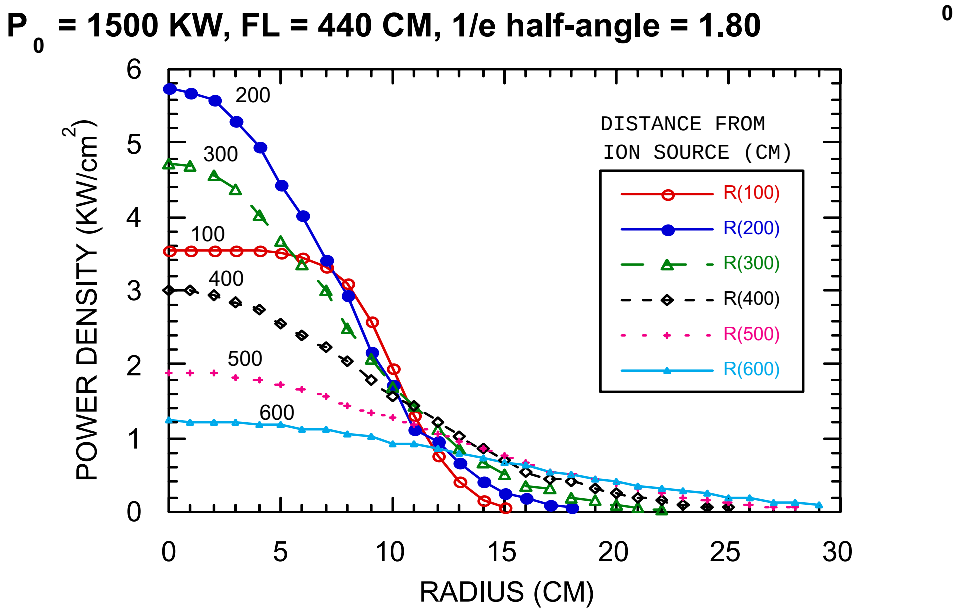

Figure 7-3. Simulated power density along beam axis. The beam port location should allow adequate duct width to avoid neutral and reionized power impingement on the duct walls

7.2.1.5 Maximizing Absorbed Power

Injected Neutral Beam power is maximized by reducing system gas pressure in the transition duct which causes reionization and loss of neutral particles. The deflection of reionized beam particles into the duct walls by the fringe magnetic field causes additional gas load from out-gassing and an avalanching of reionized power loss. Reduction of transition duct neutral gas pressure to the ~10^{-5} torr regime significantly increases injected power. This is accomplished by optimizing the duct design and installing additional cryopumping in the front box of the beamline. Table 7-2 shows the NBI system injected power capability and the effects of fringe fields.

- **PBX-M Injected Power Capability**
  - **ORNL Qualification (No Fields)**
    $H^0 \rightarrow = 6$ MW (4 x 1.5 MW)
    $D^0 \rightarrow = 8$ MW (2 x 2.0 MW)
  - **PDX Testing (No Fields)**
    $D^0 \rightarrow 8.3$ MW (4 NBI @ > 52 KV)

- **Neutral Power Reionization Loss Fractions in PBX-M Due to Duct Neutral Gas (~1-4x10^{-4} T)**
  - Perpendicular ducts → 0.88 P_0 (12% loss)
  - Tangential ducts → 0.83P_0 (17% loss)

Table 7-2. NBI power capability and reionization losses

7.2.1.6 Maximizing Desired Neutral Beam Species

Typically, neutral beamlines are operated with the neutralizer cell at ~90-95% equilibrium gas pressure to optimize the yield of the full energy component. Table 7-3 shows the measured NBI system neutral species yields. The additional gas target through the transition duct for different port access geometries can change the fractional ionic yield of the low energy components and produce small differences in the species ratios of injected beam. Small reductions in the percentage of the full energy component have been measured at the edges of beams in a narrow duct.

- **Species Measurements**
  - **H^0 @40 keV**
    - (ORNL, using ion dump yields)
      - $H^0(E):H^0(E/2):H^0(E/3) = 63:20:17$
      - $P^0(E):P^0(E/2):P^0(E/3) = 80:13:7$
  - **D^0 @ 47 keV,100 ms, 1.6 MW**
    - (PDX using RBS on injected neutrals)
      - $D^0(E):D^0(E/2):D^0(E/3) = 53:32:15$
      - $P^0(E):P^0(E/2):P^0(E/3) = 72:21:7$

Table 7-3. Species measurements for H^0 and D^0 using different methods

High duct pressure may change the species ratios measured upstream in the beamline and broaden the beam power profile. Direct species measurements of the output Neutral Beam reduce uncertainties in the analysis of experiments.

7.2.1.7 Power Transmission to the Far-Wall

Neutral Beam power transmission to the far-wall of the vessel ("shine-through") often requires at minimum sufficient armor to absorb a short full power pulse. This armor is usually designed to absorb at least a short full power pulse so as allow power and position calibration injections in the absence of plasma. Sometimes this armor is used to absorb short NBI conditioning pulses between discharges if the beamline calorimeter is not used. If far-wall armor cannot be installed, then suitable interlocks must be capable of stopping beam injection if sufficient plasma is not present. A useful formula for calculating the approximate fraction of beam that will "shine-through" a PDX plasma (R. Goldston) is:

H^0: 50 keV/nucleon ~ $3.4 \times 10^{-16}\ \text{cm}^{-2}$

$$\text{Shine-thru} = \exp(-n_e \bullet 90 \bullet 3.4 \times 10^{-16}) = \exp(-n_e / 10^{13} \bullet 0.31)$$

D^0: 25 keV/nucleon ~ $7.4 \times 10^{-16}\ \text{cm}^{-2}$

$$\text{Shine-thru} = \exp(-n_e / 10^{13} \bullet 0.67)$$

Figure 7-4 shows a plot of transmission through PDX plasmas *versus* density for H^0 and D^0 at 40 and 50 keV.

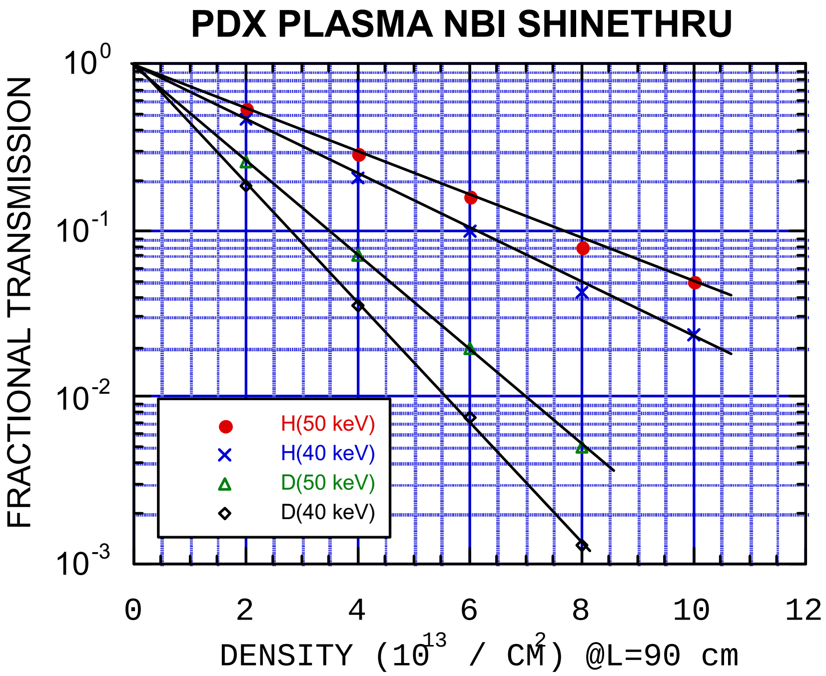

Figure 7-4. Plot of Neutral Beam power fractional transmission through a 90 cm thick PDX plasma *versus* density. This corresponds to the case of near-perpendicular injection (RTAN = 35 cm)

These results indicate that, for example, ATJ graphite at least 1.3 cm thick or the equivalent will be sufficient for wall armor tiles capable of absorbing the available peak NBI power densities of 3 kW/cm^2 for 500 msec in the absence of plasma. Thicker tiles with active cooler will be needed as an upgrade for longer NBI pulse lengths.

7.2.1.8 Minimizing Duct Wall Conditioning

Gas absorbed on and in duct walls is released (outgasses) under particle bombardment and heating. The reduction of duct outgassing by conditioning increases injected power and provides more reproducible results. Figure 7-5 shows the measured PDX East NBI system duct outgassing versus the cumulative power absorbed over several months. It is seen that, initially at the beginning of a 1-2 week Run, the duct outgassing was high but decreased steadily during the Run. Interruption of the Run for Maintenance resulted in the return of high outgassing rates due to fresh gas adsorbed on the duct walls from the vessel, and volume diffusion of fresh gas to the surface of the duct walls to replenish the outgassed surface region.

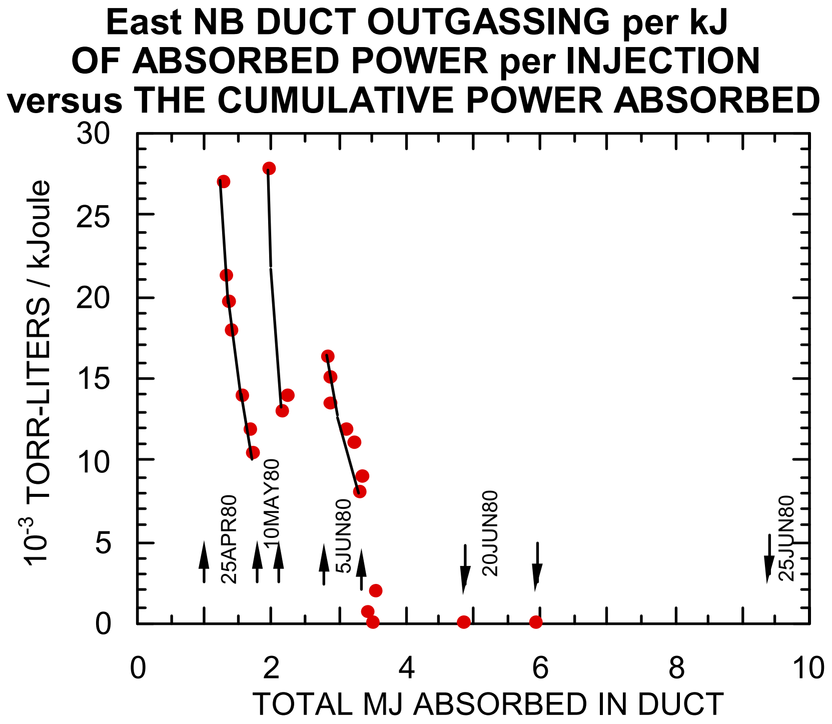

Figure 7-5. Measured duct outgassing during several months of operation. H2 Glow Discharge Cleaning (GDC) was used to clean the vessel immediately after pump-down from a vent. No H_2GDC or other GDC was applied thereafter. The application of HeGDC in the transition duct prior to NCSX daily operations and between discharges would reduce duct conditioning time significantly.

Duct outgassing can be reduced by high conductance geometry, with walls far from the beam, appropriate materials, baking, and HeGDC between discharges. The NCSX design will include the installation of high-speed cryopumping in the exit box of the beamlines at the entrance to the duct to significantly reduce or eliminate the effects of duct outgassing. This hardware will also accelerate NCSX pumpdown between discharges.

7.2.2.1 NCSX NBI Duct Design Optimization and Port Access Requirements

The NBI port access requirements discussed above can be summarized by reference to Figure 7-6, which shows a schematic diagram of the principal elements of a high conductance NBI transition duct. The beam, after passing through the beamline Torus Interface Valve (TIV), enters a rectangular section which is usually connected to a cylindrical section attached to the vessel. In the case of PBX-M, reionized power loss due to residual process gas in the duct is steered to the duct side wall by the predominantly vertical fringe field at the entrance to the duct, and eventually to the top of the duct by the predominantly horizontal fringe field at the vessel entrance. The duct has a ceramic break providing electrical isolation of about 3 kV, and a bellows at the vessel to decouple vessel motion during operation and bakeout. The bellows is shielded with a metal sheet fastened to the vessel and floating on the beam side. Diagnostic ports are provided to provide viewing of the beam in the duct for NBI and plasma related measurements (e.g., BES calibrations).

Optimization of the duct design consists in maximizing the width W, the height H, and the diameter D, while minimizing lengths Lr and Lc. The use of electropolished 304-SS (stainless steel) reduces the ratio of the atomic-to-geometric surface areas of the walls, which reduces outgassing. If possible, the use of a rectangular ceramic break and a rectangular bellows will maximize the vacuum pumping conductance. All vacuum seals will be bakeable to 150°C, to implement a 150°C bakeout capability, and possibly, to operate with the duct walls at 150°C. There will be a port for a duct ion gauge to monitor reionized power losses, and other diagnostic ports with spool pieces so as to avoid the direct impingement of reionized power on port flanges.

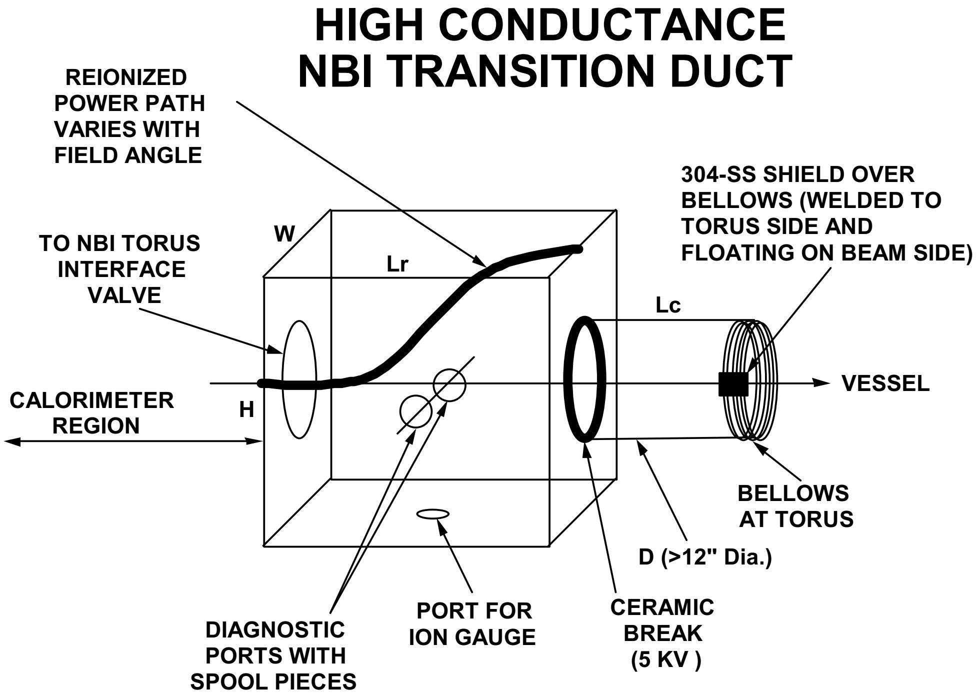

Figure 7-6. A partial schematic diagram showing the principal elements of a high conductance NBI transition duct

The NCSX design will include a duct port dedicated to a GDC electrode to facilitate duct conditioning. Table 7-4 gives a summary of the NBI transition duct and port requirements. The far-wall beam armor design will also include beam power and position diagnostics.

- Maximize dimensions W, H, and D (min. ~12”).
- Use electropolished 304-SS.
- If possible, use rectangular ceramic break and bellows to maximize conductance.
- All vacuum seals bakeable to 150°C.
- Provide 150°C bakeout capability.
- If possible, useful to operate at 150°C.
- Provide ion gauge port.
- Provide diagnostic ports with spool pieces.
- Provide port for GDC electrode.
- Far-wall beam armor should have beam diagnostics

Table 7-4. Summary of NBI transition duct design optimization and port access requirements

Hence, synergies accrue from combining duct requirements of the Neutral Beam and Torus Vacuum Pumping Systems. Figure 7-7 shows a schematic diagram of the principal

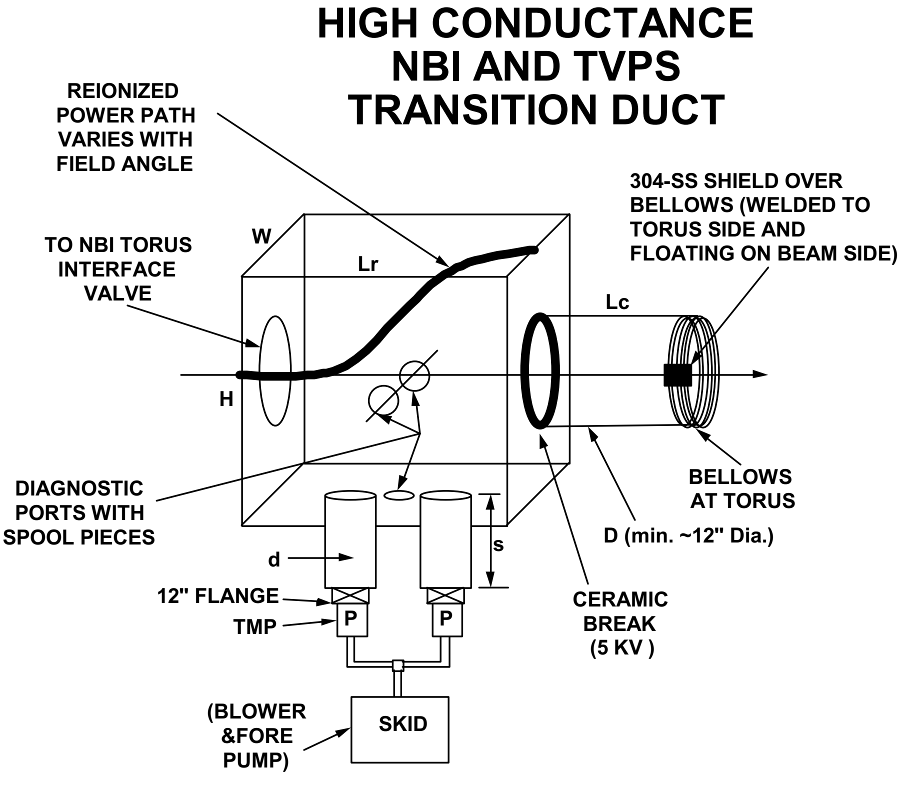

Figure 7-7. A partial schematic diagram showing the principal elements of a high conductance transition duct that combines the requirement of both NBI and TVPS requirements.

elements of a high conductance NBI transition duct that combines the design requirements for the Neutral Beam and Torus Vacuum Pumping Systems.

The proposed duct design (Figure 7-7) is essentially that discussed above with the addition of a Torus Vacuum Pumping System (TVPS) turbo molecular pumping station. It has maximized the width W, the height H, the diameter D and the diameter d, while minimizing lengths Lr and Lc. Length S is selected for high conductance reaching a fringe field region comparable to that at the pumps during their PBX-M service. In addition, S is sufficiently long to provide occlusion from beam sputtering. The other requirements discussed above are also applicable (electropolished 304-SS walls, 150°C bakeout capability). Table 7-5 gives a summary of the NBI transition duct, TVPS, and port access design optimization requirements.

- Port Access and external constraints need to be varied to:
    - Maximize dimensions of H,W, D
    - Minimize dimensions of Lc, Lr
    - Select S for high conductance, B-field operation, and occlusion from beam sputtering
    - Provide bakeability

Table 7-5. Summary of the NBI transition duct, TVPS, and port access design optimization requirements

7.2.2.2 NCSX NBI Design Maximizes Absorbed Power

The NCSX design locates the NBI ports so as to maximize the absorption of injected beam power over the desired plasma region. The absorbed power is determined by the beam focusing (perveance), the distance of the ion source from the deposition region, the aiming angle, and target plasma parameters.

7.2.2.3 NCSX NBI Design Maximizes the Desired Injected Species

The NCSX design locates the NBI ports so as to minimize effects on injected neutral particle species. Neutral Beam ion sources produce three ionic species [$H^+(E)$, $H^+(E/2)$, $H^+(E/3)$, or $D^+(E)$, $D^+(E/2)$, $D^+(E/3)$]. The ion source and neutralizer, which are operated so as to maximize the full energy operation, determine the net neutral species fractions entering the transition duct [$H^0(E)$, $H^0(E/2)$, $H^0(E/3)$, or $D^0(E)$, $D^0(E/2)$, $D^0(E/3)$].

7.2.2.4 NCSX NBI Design Allows Far-Wall Armor to Absorb Beam Shine-thru

The NCSX design locates the NBI ports so as to minimize beam power deposition on ports on the opposite wall. The port locations will allow the mounting of far-wall armor to absorb shine-through power and allow full-power, short-pulse beam injections in the absence of plasma for calibrations. Hence, far-wall armor provides wall protection and functions as an instrumented NBI diagnostic (IR Camera viewable, thermocouples, and/or water calorimetry).

7.2.2.5 The NSCX NBI Design Accommodates In-Vessel Constraints

The NCSX NBI port locations will allow for RF Antenna positioning requirements and special diagnostic location requirements. The requirements pertaining to the deposition of absorbed NBI power are addressed above. This will involve avoiding the direct NBI aiming at a port, but if this is not possible, the width of the required NB in-vessel armor can be extended into the duct entrance. Other constraints may pertain to toroidal location (e.g., plasma shape, Beam orbit loss deposition), and diagnostic relationships (*e.g.*, optical and IR views, the proximity to RF Antennas of magnetic diagnostics for control and MHD measurements, *etc.*).

7.2.2.6 NCSX Co & Counter NBI Configurations

Balanced co- and counter-tangential NB injection is needed to provide control of the neutral-beam driven currents, as discussed in Chapter 10, and to provide control of the driven rotation (and thus electric field) for transport studies. Configurations for 2 Co and 2 Counter NBI configurations have been studied using the constraints listed above in Sections 7.2.2.1 – 7.2.2.5. Figure 7-8 shows a candidate configuration for 2 Co and 2 Counter NBI system in the combined Test Cell. The planed site layout will also accommodate beam configurations with three co- and one counter-injected beam.

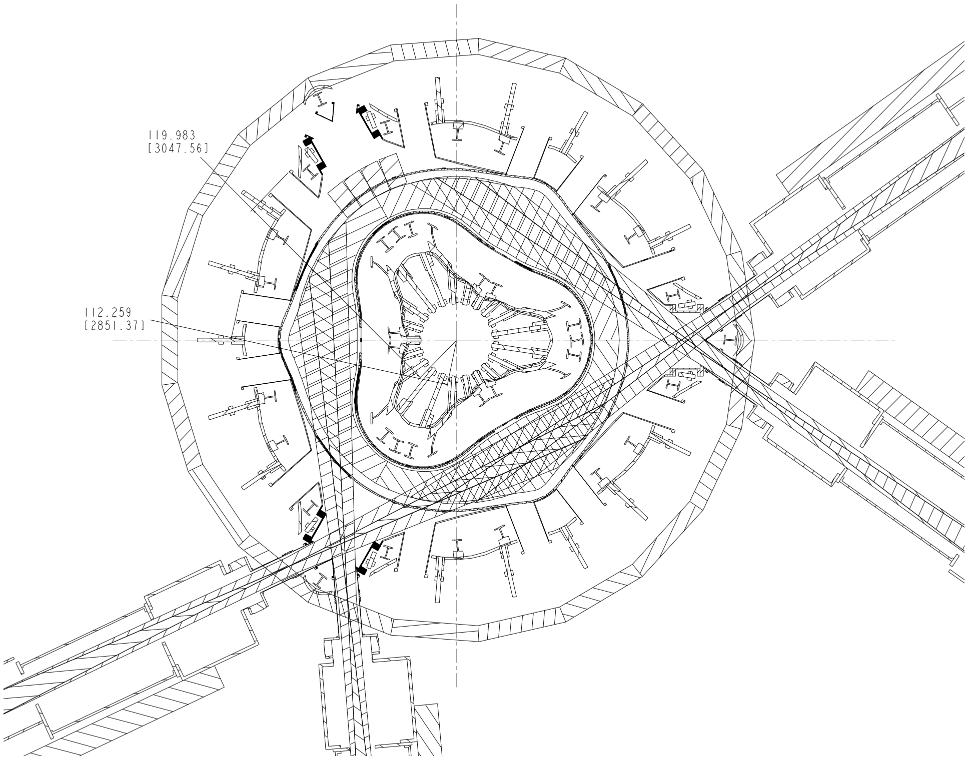

Figure 7-8. Candidate configuration for 2 Co and 2 Counter NBI system

A critcal element in this configuration is the transition duct region. Each transition duct region is shared by 2 beamlines ,and nearby walls receive power from an oppositely directed NBI. Figure. 7-9 shows one possible conceptual design of a transition duct region consistent with the principles given above.

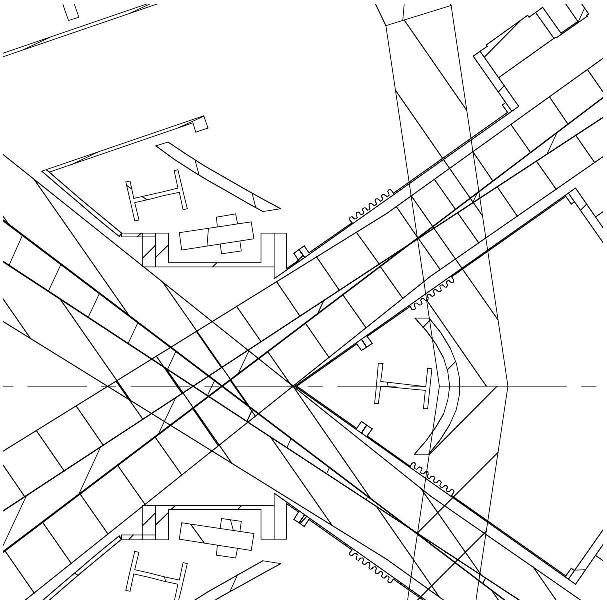

Figure 7-9. Conceptual design of a transition duct region

7.3 Fast Ion Confinement Analysis for NCSX

7.3.1 Introduction

Neutral beams will provide one of the primary heating methods for NCSX; up to 6 Mw of beam power will be available in the 40 to 50 keV energy range. These beams will be injected tangentially in both the co- and counter- directions in order to minimize beam driven currents. In addition to plasma heating, beams are also expected to provide a means for external control over the level of toroidal plasma rotation velocity and its profile.

NCSX has been designed to be as toroidally symmetric as possible in magnetic Boozer coordinates.[1] This leads to improved energetic beam ion confinement and higher predicted heating efficiencies in comparison to more conventional stellarators. However, even in such an optimized stellarator, there will remain some non-zero departure from perfect symmetry. These deviations will lead to somewhat enhanced levels of beam ion losses above those present in an equivalent symmetric tokamak. For example, localized magnetic wells in the stellarator can result in small fractions of locally trapped orbits that drift directly out of the plasma; this ripple can additionally cause banana orbits trapped in the 1/R wells to gradually leave the plasma due to the successive perturbations in their bounce points. Barely passing particle orbits are also perturbed by low levels of this ripple; their orbits can become stochastic over many toroidal transits and leave the plasma.

The above orbital effects require careful analysis for neutral beam heating since they are especially exacerbated by the nearly collisionless nature and high transit speed of the beam ions. This forms the motivation for the following set of calculations. The model described below is used for estimations of beam heating efficiencies (important for plasma performance estimations), scaling of heating efficiency with machine size and magnetic field level, parameter studies of the optimum beam injection tangency radius and toroidal injection location, and loss patterns of beam ions on the vacuum chamber wall (important for placement of wall armor and for minimizing the generation of impurities by the energetic beam ions).

7.3.2 Description of Model

Our model (the DELTA5D[2] code) is based on the geometry shown in Figure 7-10. A pencil beam (zero width) is injected into the plasma on the equatorial plane ($\theta = 0$) aimed at a particular toroidal angle $\zeta_{inj.}$ and tangency radius, R_{tan} which can be varied. The deposition profile for the beam is externally specified and is obtained from the modeling of similar axisymmetric systems (using the cross-sectional shape at the $\zeta = \pi/3$ plane) using TRANSP[3]. Particles are initially distributed over flux surface locations in consistency with this deposition profile. Only flux surfaces having major radii (at $\theta = 0$) > R_{tan} are populated with beam ions. The initial beam ion pitch angle distribution in $v_{\|}/v$ is then determined by taking the ratio of the beam tangency radius to the local value of major radius where the particle is born.

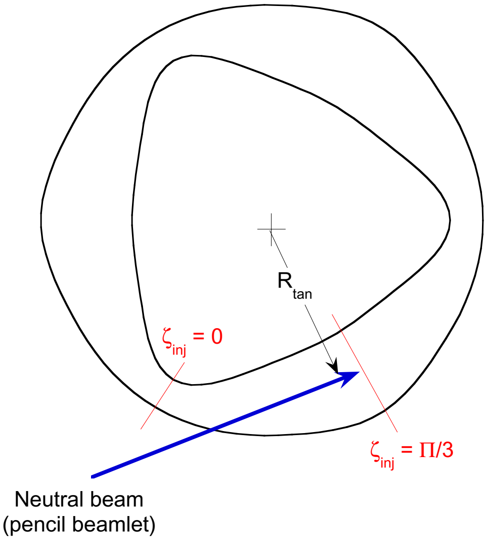

Figure 7-10. Geometry used for NCSX neutral beam calculations

From these initial conditions, the beam particle orbits are then followed by solving Hamiltonian guiding center equations which time advance the particles in the two angular coordinates (poloidal and toroidal angles in Boozer coordinates) and the conjugate momenta. Equilibrium magnetic fields are obtained from the VMEC stellarator equilibrium code[4] which are then transformed to Boozer coordinates.[1] Collisions with a static background plasma consisting of electrons and two background ion species (a main ion and one impurity component) are simulated using a Monte Carlo collision operator[5] based on pitch angle and energy scattering terms, taking into account the full velocity-dependent potentials[6] without assumptions regarding relative orderings of the electron, beam ion and impurity velocities. Collisions are allocated on a fixed time step Δt_{coll} which is chosen so as to maintain $\nu\Delta t_{coll} << 1$ and to allow a smooth granularity in modeling the collisional processes. The time integration step for the orbit integration is controlled by the ordinary differential equation solver LSODE[7] which internally choses an integration time step so as to maintain a prescribed accuracy level. The typical variation of the different beam ion collision frequencies with velocity and flux surface included in this model are shown, respectively, in Figures 7-11(a) and 7-11(b).

The subscripts on the collision frequencies denote the species (electrons, ions, impurities) which the beam is colliding with and whether the collision frequency pertains to pitch angle deflection (D) or energy scattering (E). Currently we do not include collisions with neutrals. Typically, the beam ions are injected at a velocity where they are slowing down somewhat more

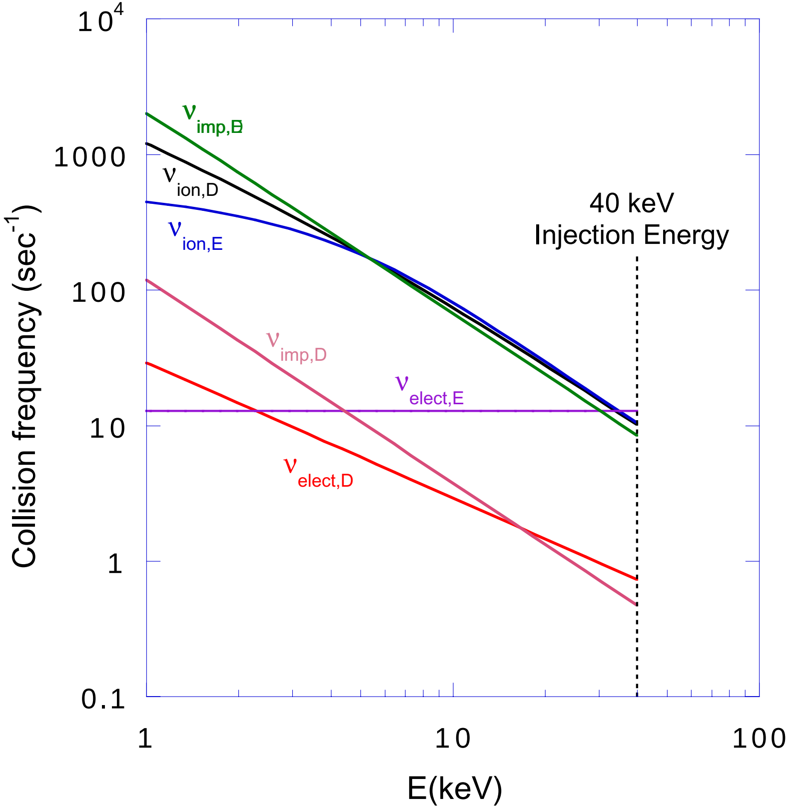

Figure 7-11(a). Collision frequencies vs. energy at r/a = 0.5 (collision frequencies with D/E subscripts denote pitch angle/energy scattering rates, respectiveley; ion, elect, imp subscripts denote beam collsions with plasmas ions, electrons, and impurities)

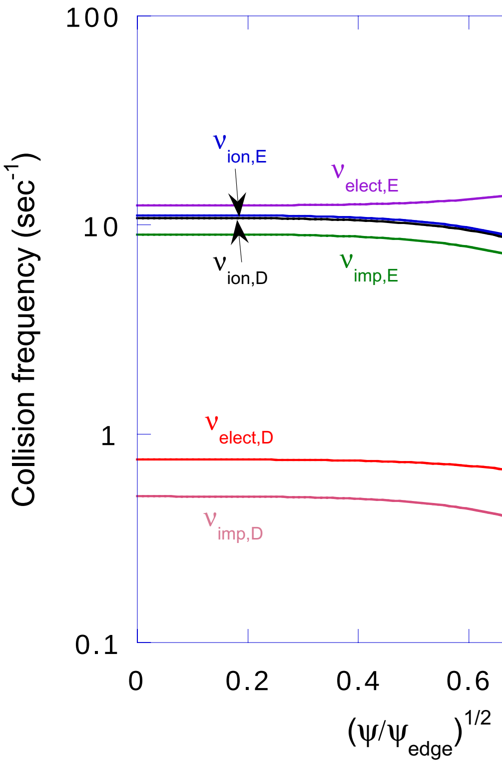

Figure 7-11(b). Collision frequencies vs. flux surface at E = 40 keV (collision frequencies with D/E subscripts denote pitch angle/energy scattering rates, respectiveley; ion, elect, imp subscripts denote beam collsions with plasmas ions, electrons, and impurities)

on electrons than ions, but they soon pass through the critical energy, below which they begin slowing down more on ions. Also as the beam ions pass through the critical energy, pitch angle scattering begins increasing; this can result in higher fast ion losses as the ions get scattered out of the passing region of velocity space. As the beam ions slow down to 3/2 kT_{ion} (with T_{ion} being the background field ion temperature), they are counted as part of the background plasma species. Beam ions that pass through the outer flux surface are removed from the distribution and not replaced; thus, the quoted loss rates may be a slight overestimate. Beam heating efficiencies are calculated by recording the losses of particles and energy out of the outer magnetic flux surface that occur during the slowing-down process. The DELTA5D2 code follows groups of beam particles on different processors in parallel using the MPI language for inter-processor communication. It has been adapted to both the Cray T3E and IBM-SP computers. A variety of diagnostics of the escaping particles, such as pitch angle, energy and particle lifetime distributions, are retained to aid in understanding the loss mechanisms.

In Figures 7-12(a) and 7-12(b) we show some of the characteristics of a slowing-down beam for the parameters $n(0) = 6 \times 10^{19}$ m^{-3}, $T_e(0) = T_I(0) = 2.4$ keV. Figure 7-12(a) shows on the left-hand scale the time evolution of the percentage of energy lost from the beam averaged over the ensemble of 4,096 particles used here. We normally follow the distribution of beam particles until this energy loss fraction reaches a saturated plateau; this flattening is associated with the average beam ion slowing down to the 3/2 kT_{ion} energy level [shown on the right-hand scale in Figure 7-12(b)]. Figure 7-12(a) also shows the time variation of the ensemble averaged ratio of magnetic moment to energy for the beam. Initially this ratio starts out small due to the anisotropic nature of the beam (i.e., composed mostly of passing orbits) and then increases as the beam pitch angle scatters and spreads out to become more isotropic. Finally, Figure 7-12(b) shows the decrease in time of the number of beam particles, indicating the degree to which particles are lost at times prior to that required for slowing down enough to join the background distribution.

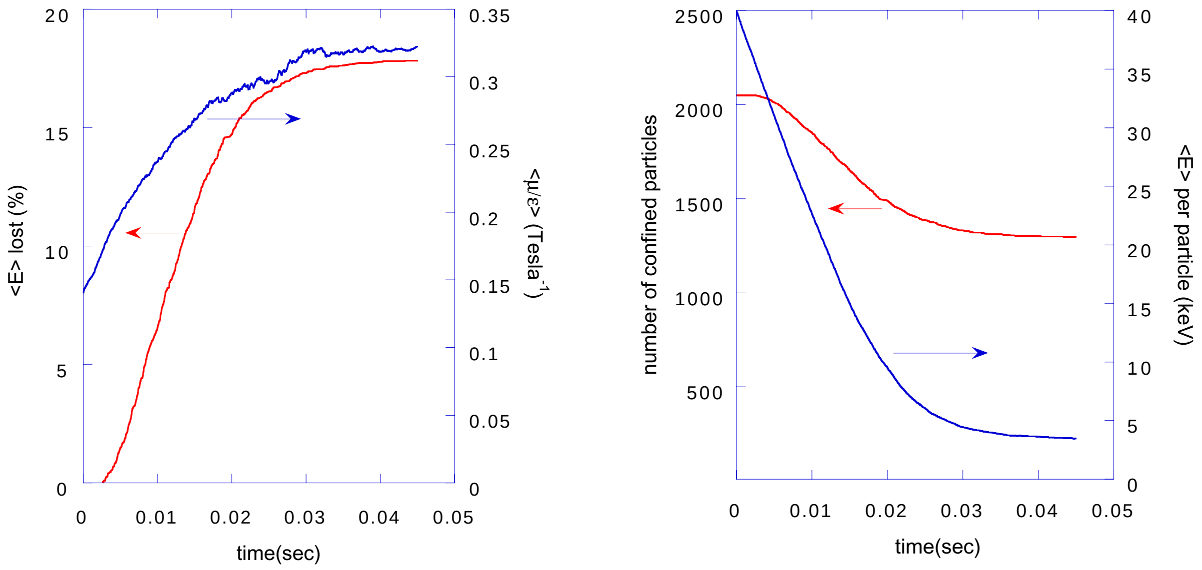

Figure 7-12(a). Typical evolution of ensemble averaged beam energy loss and $<\mu/\varepsilon>$; (b). Decay in time of the number of confined beam particles and average energy per particle

Figures 7-13(a) and 7-13(b) show histograms of the energy and pitch angle distributions of the escaping beam ions for the case shown in Figure 7-12. As can be seen, the energy losses are characterized by a broad peak centered around 15 - 20 keV for both co- and counter- injection. The counter-injected ions also show a very sharp peak at the injection energy, presumably associated with prompt losses. The pitch angle distributions of escaping ions shown in Figure 7-13(b) are mostly peaked around the deeply trapped range of pitch angles with a secondary peak (for the co-injected ions) more in the transitional region. The counter-injected ions show a very sharp peak near $v_{\|}/v = 0.6 - 0.7$ which is close to the birth pitch angle, indicating a prompt loss component for the case of a tangency radius $R_{tan} = 1.7$ m.

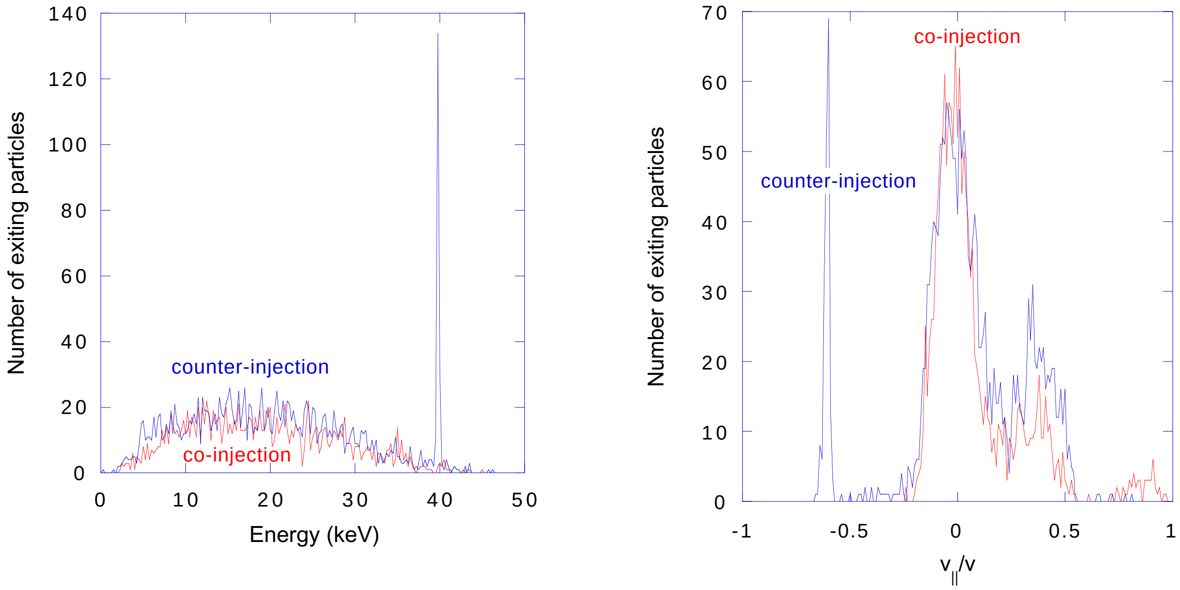

Figure 7-13(a). Energy spectrum of exiting beam particles; (b). Pitch angle spectrum of exiting beam particles

7.3.3 Parameter Scans

We have used the model described above to study sensitivity to variations in configuration, beam and plasma parameters. In Figures 7-14, 7-17 through 7-19, we have used an earlier sizing of NCSX,[8] LI383, with a volume averaged magnetic field of 2 Tesla, and an average major radius of 1.7 meters. The central plasma density is nominally 6 x 10^{19} m^{-3} and the central ion and electron temperatures are set to 2.4 keV; the plasma species is hydrogen. An impurity species is present with Z = 18, A = 9, at 1% of the electron density, and a temperature equal to the background ion temperature. The beam is also taken as hydrogen and is monoenergetic at injection with an energy of 40 keV. The beam is initially deposited at $\theta_{inj} = 0$, $\zeta_{inj} = \pi/3$. Plasma profiles for temperature and density go as $1 - \psi^2$ and the ambipolar potential is set to zero. In the results for Figures 7-15 and 7-16 we have used the same configuration, although with design point parameters chosen for $R_0 = 1.4$ meters and <B> = 1.23 Tesla; temperatures and densities for these cases are based on transport modeling.

In Figure 7-14 the sensitivity of losses to the beam injection angle and tangency radius for co- and counter-injected beams in a <B> = 2T and $R_0 = 1.73$ m device is examined. In Figure 7-14(a) the toroidal angle at which the beam ions are initially deposited is varied, going from the beginning of the field period ($\zeta_{tan} = 0$ symmetry plane) to the half field period point ($\zeta_{tan} = \pi/3$); these two angles have been shown in Figure 7-10. Beam losses only depend weakly on the injection location due to the fact that most losses only occur after many transits around the stellarator after which collisions presumably will have spread out the beam distribution more uniformly in toroidal angle and erasing any memory of the initial particle loading. Nevertheless, there is some variation of losses with changes in ζ_{tan} and it appears that there is an optimum around $\zeta_{tan} = \pi/4$ for both co- and counter-injected beams. The reasons for this slight minimum in losses have not been investigated yet, but are expected to be caused by the dependencies of the first orbit losses on the injection angle.

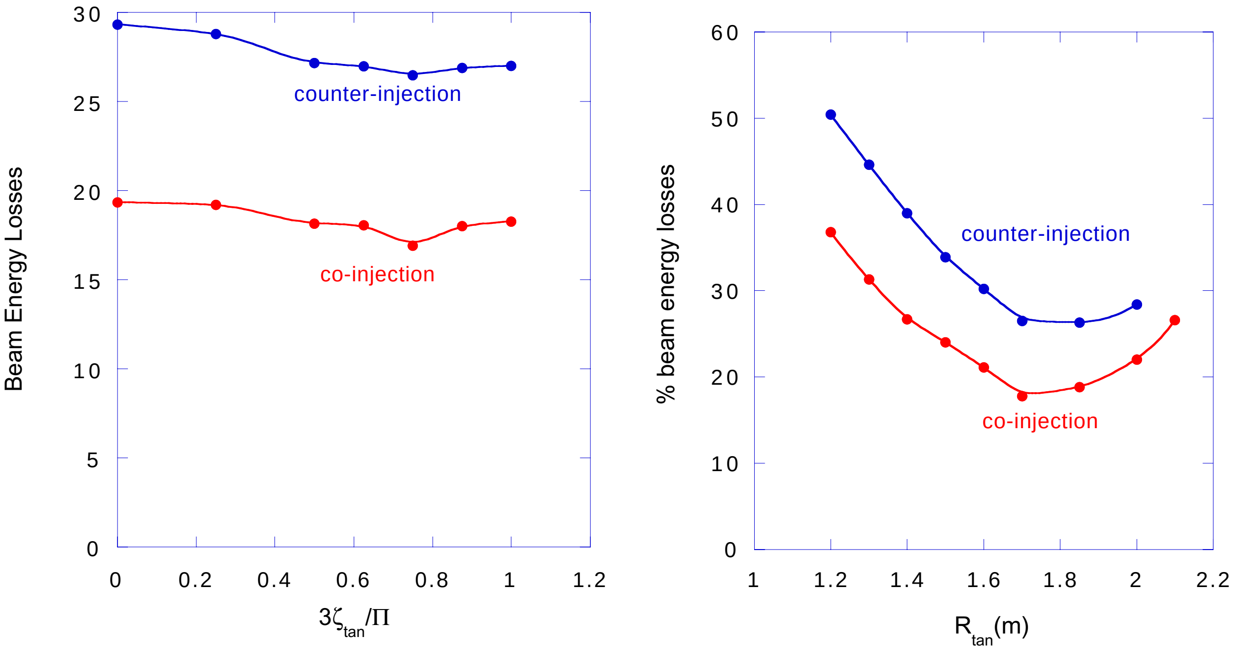

Figure 7-14(a). Dependence of beam losses on toroidal injection location; (b). Dependence of beam losses on beam tangency radius for a version of NCSX with R_0 = 1.73 m.

In Figure 7-14(b) the tangency radius for injection is varied. As the tangency radius is made smaller, the beams are initially launched onto larger pitch angles relative to the magnetic field (smaller $v_{||}/v$). This puts them closer to the trapped-passing transitional regime of velocity space where orbits are more likely to experience prompt losses. As may be seen, the losses steadily increase for both co- and counter injected ions as R_{tan} is decreased. The minimum of these curves is close to the point where R_{tan} = the magnetic axis location. For this configuration the magnetic axis at the toroidal injection angle ($\zeta_{inj} = \pi/3$) was 1.68 m. As R_{tan} is increased beyond this point, losses again increase due to the fact that the beam ions are progressively being aimed further out in minor radius leading to hollow deposition profiles and increased fractions of prompt orbit losses. For subsequent analysis, the injection angle was chosen so that $\zeta_{tan} = \pi/3$ to best matches the beam and plasma cross section. The tangency radius is taken to be the magnetic axis location.

In Figure 7-15 we investigate the variation of beam losses with injection. Results presented in the previous Figures have been based on a 40 keV injection energy. The beams anticipated for NCSX will be capable of going up to 50 keV, but will also include lower energy components. For Figure 7-15, we have also shifted our plasma and machine parameters to the planned experiment with R_0 = 1.4 meters, <B> = 1.23 Tesla, average temperature for ions and electrons = 1.26 keV and average electron density = 6.8 x 10^{19} m^{-3}; these correspond to peak temperatures and densities of 1.58 keV and 8.5 x 10^{19} m^{-3} respectively (here we have used profiles that go as $1 - \psi^2$). Although the device size and magnetic field strength are smaller for this case, the beam losses are also lower due mostly to the fact that the slowing down time is shorter for these parameters. Another factor which keeps beam losses lower here is that the critical energy (E_{crit}) where the fast ions begin slowing down more on background ions than electrons is lower. For these parameters, it is around 23 keV while for the earlier parameters [$n(0) = 6 \times 10^{19}$ m^{-3}, $T_e(0) = T_I(0) = 2.4$ keV], E_{crit} was around 34 keV. This lower E_{crit} also is likely to account for the fact that beam losses seem to actually get slightly lower with increasing energy for the co-injected beams from 30 up to 50 keV. This is caused by the fact that below E_{crit} pitch angle scattering rapidly increases resulting in beam ions being scattered into the more lossy transitional and trapped orbits. As the initial beam energy is increased above E_{crit}, the beam ions can undergo more energy slowing down without as much pitch angle scattering, resulting in a smaller proportion of the initial beam energy being lost through scattering into unconfined orbits. In Figure 7-15 we show results both for (a) hydrogen beams injected into a hydrogen plasma, and (b) deuterium beams injected into a deuterium plasma.

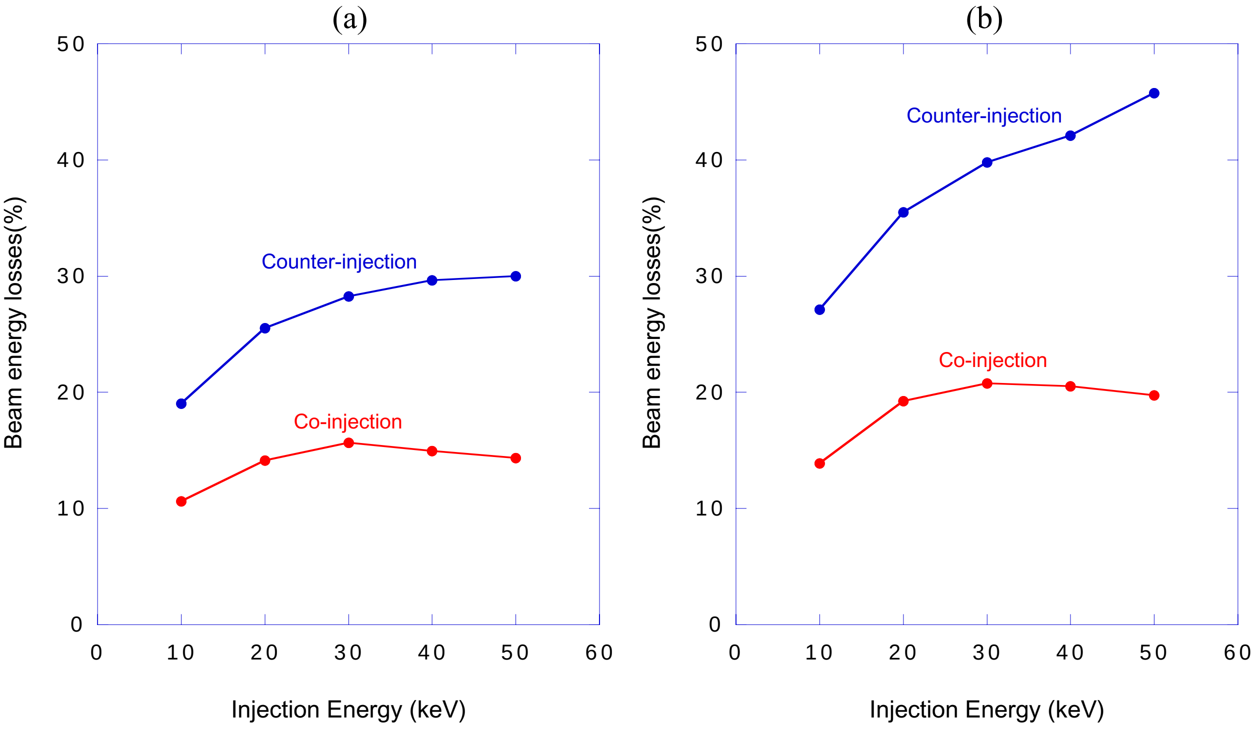

Figure 7-15. Variation of the beam energy losses with injection energy for a recent machine design point at $R_0 = 1.4$ m, $\langle B \rangle = 1.23$ T, $n(0) = 8.5 \times 10^{19}$ m^{-3}, $T_e(0) = T_I(0) = 1.58$ keV for (a) Hydrogen beams injected into a hydrogen plasma, and (b) Deuterium beams injected into a deuterium plasma

In Figure 7-16 we examine the variation of beam losses as the magnetic field is changed, using the $R_0 = 1.4$ m device and 40 keV beams. Here we have used profiles for temperature for temperature and density obtained from transport modeling with $n(0) = 8.1 \times 10^{19}$ m^{-3}, $T_i(0) = 1.9$ keV, $T_e(0) = 2.9$ keV.

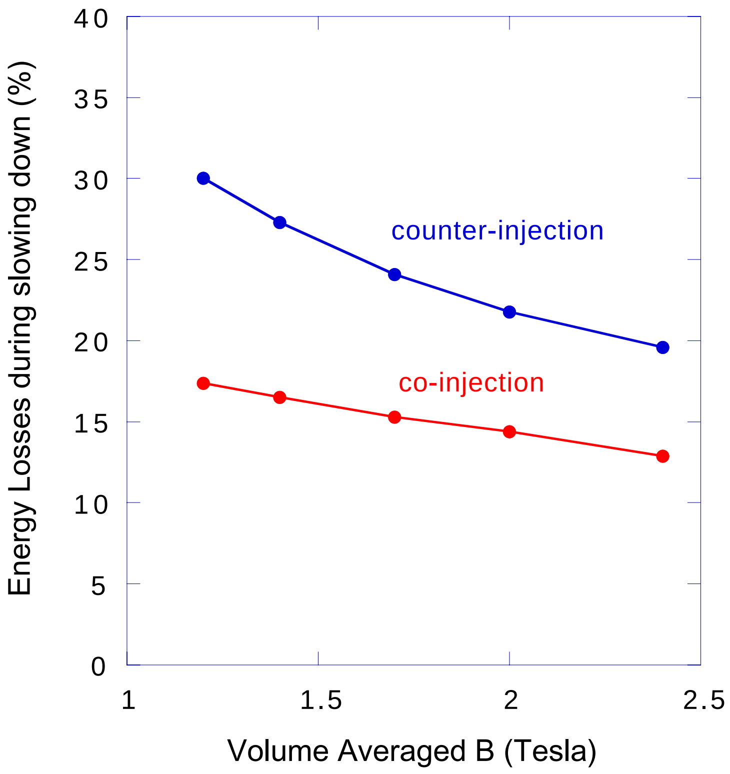

Figure 7-16. Variation of beam losses with magnetic field for 40 keV hydrogen ions for a device with R_0 = 1.4 meters

The results shown in Figure 7-16 at <B> = 1.23 Tesla have also been used in the transport predictions of Chapter 8.

7.3.4 Loss Patterns of Beam Ions on Outer Flux Surface

As indicated in Figure 7-13(a), a large fraction of the escaping beam ions leave the plasma with 1/3 to 1/2 of their initial injection energy. It is desirable to intercept this power deposition on the vacuum chamber wall by localized protective armor plating to minimize impurity generation and wall erosion. In order to design such structures, it is necessary to make estimates of the wall locations where the escaping beam ions will be deposited. Within the above Monte Carlo model, as the beam ions leave the outermost closed flux surface, their exit locations, exit times, pitch angles and energies are recorded. If it is assumed that beam ions then move rapidly through the unclosed outer flux region, this information can be useful in estimating power loading patterns on the vacuum chamber walls. More realistic models may eventually be developed which follow the fast ion trajectories in the outer region where flux surfaces no longer exist. Results based upon the current model are shown in Figure 7-17 for a typical case. Here the exit locations are plotted in Boozer poloidal and toroidal angle coordinates for the outermost flux surface. Colors are used to indicate the energy at which the fast ions leave the surface. As can be seen, most of the ions leave at intermediate energies from 10 - 20 keV, in similarity with Figure 7-13(a).

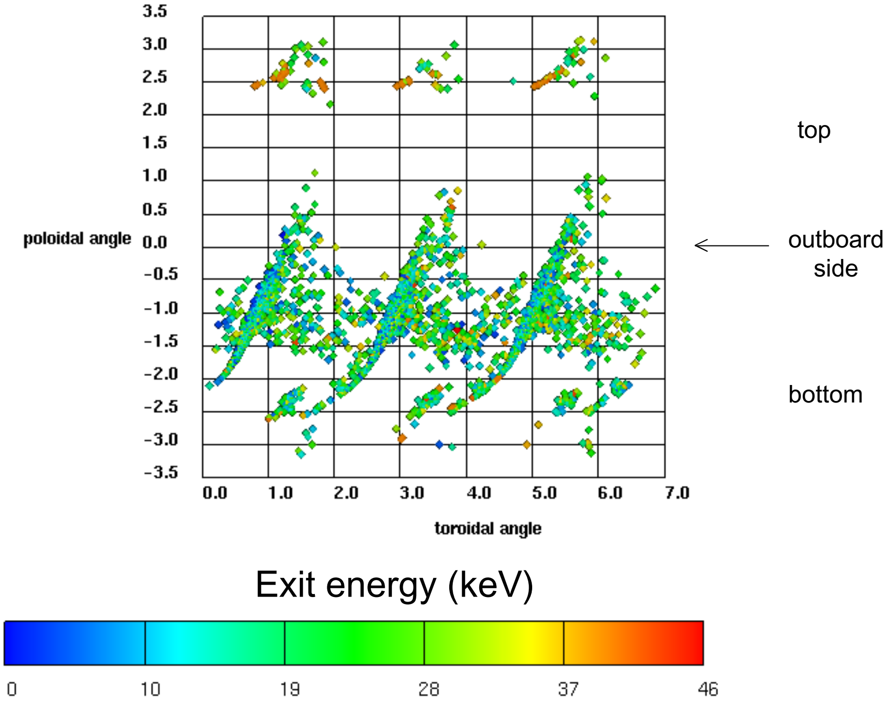

Figure 7-17. Location and energy spectrum of beam losses on outer surface in 2D Boozer coordinates

The fast ion losses are primarily concentrated in helical stripes on the bottom of the stellarator with one stripe per field period (this would presumably shift to the top of the stellarator with reversal of the magnetic field direction). We have also transformed this data into more geometric coordinates. In Figure 7-18 we plot the data of Figure 7-17 vs. the normal cylindrical azimuthal coordinate, $\phi_{cylindrical}$ and a poloidal angle, θ, which is equal to $\tan^{-1}[z/(R-R_0)]$.

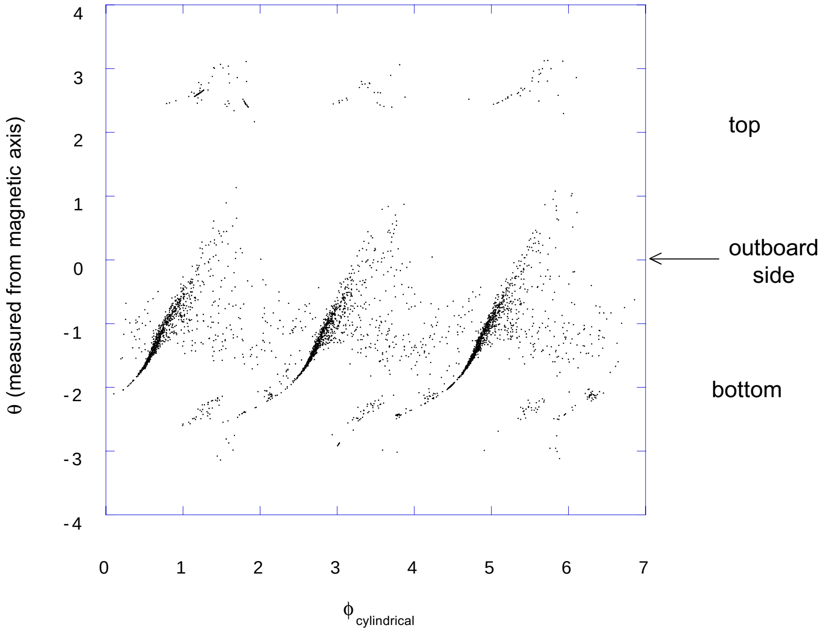

Figure 7-18. Location of beam losses on outer surface in 2D real space coordinates

Finally, we have plotted the ion loss locations on the three-dimensional outermost flux surface (Figure 7-19) as obtained from the VMEC stellarator equilibrium code. The flux surface is shown in red and the ion exit locations are color coded according to the ion's energy at the time it passes through the flux surface. Again, it can be seen that the losses are somewhat concentrated, motivating the design of protective structures at these locations. These issues will be further discussed in Chapter 11.

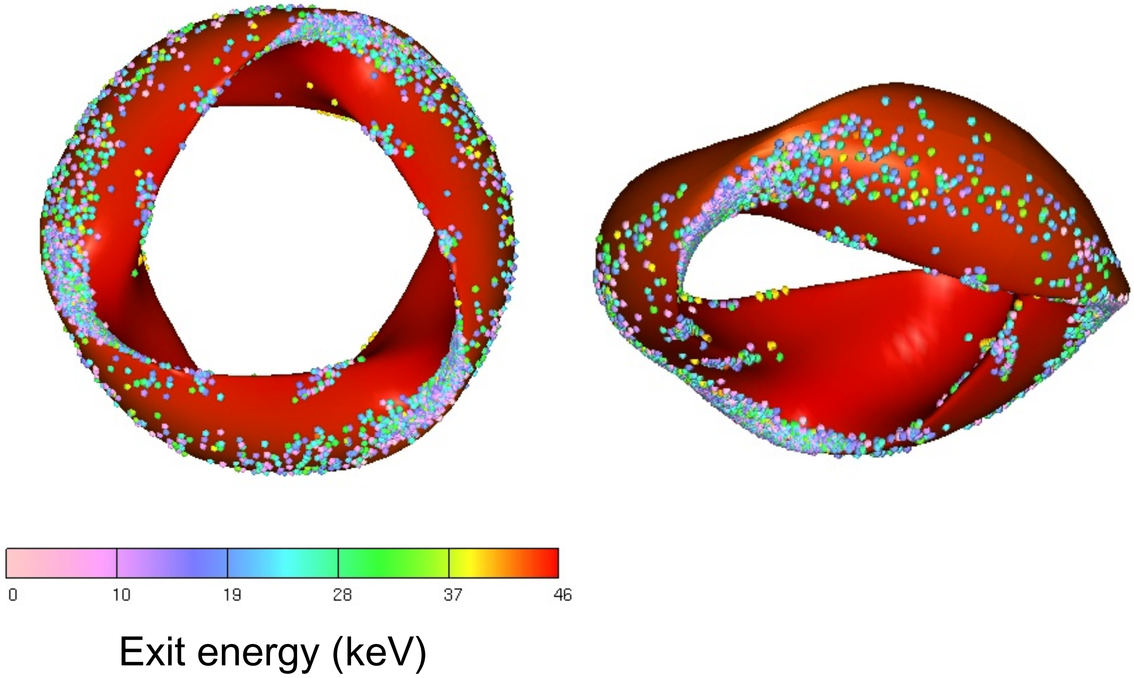

Figure 7-19. Location and energy spectrum of beam losses on outer surface in 3D

7.3.5 Suggestions for Future Work

The model described here has been developed for comparative studies of different NCSX configurations and to obtain approximate estimates of beam heating efficiencies and loss patterns. In order to develop an adequate physics understanding of fast ion confinement in a real experiment, a number of upgrades and new tools will need to be developed. Although many of these issues have already been thoroughly examined for tokamaks, the inherently 3D nature of the stellarator geometry will, in many cases, require a complete re-development of existing tools.

In the area of neutral beam deposition, finite width, multiple energy group beam models will need to be developed and their intersection with the 3D flux surface shapes taken into account. As the beam ions slow down, collisions with neutrals and multiple impurity species should be modeled; beam-beam self collisions and finite beam gyroradius effects may also be of relevance for some regimes. A number of additional physics diagnostics for beam ion effects can readily be included in the Monte Carlo calculations. For example, beam-driven currents and transfer rates of beam energy to the different plasma species can be obtained. Other diagnostics, such as predictions of the energy distributions of charge exchange neutrals escaping the plasma, can be useful in interpreting charge exchange measurements.

The beam slowing down model described here assumes nested, closed flux surfaces. Stellarators can develop magnetic islands and open field lines at some point near the plasma edge. In determining beam loss rates through these regions as well as beam loss patterns and heat loads on walls and divertors, it could be important to follow beam ion orbits into these regions by matching together Hamiltonian orbit models for the inner closed surface region with more conventional real space guiding center drift models for the regions outside the last closed flux surface.

7.4 High Frequency Fast Wave Heating

7.4.1 Introduction

The RF heating system for NCSX will be designed to deliver 6 MW of radio frequency (RF) power to the plasma. The baseline technique chosen for RF heating is High Frequency Fast Wave (HFFW) heating. HFFW is closely related to High Harmonic Fast Wave (HFFW) heating, which has recently been applied in the National Spherical Torus eXperiment (NSTX). HHFW, like HHFW, utilizes fast magnetosonic waves at high harmonics of the ion cyclotron frequency, which minimizes ion damping while producing strong damping on the electron population. However, because of the higher confining magnetic field in NCSX, compared to NSTX, operation at high harmonics in NCSX implies much higher absolute frequencies. The operating frequency chosen for NCSX is 350 MHz. This choice of frequency dictates the use of klystrons for power sources, and folded-waveguide launchers for coupling RF to the plasma.

One of the primary drivers for the choice of HFFW heating for NCSX was launcher accessibility to the plasma, compatible with the earlier coil designs. Accessibility restrictions have relaxed with the design change to modular coils. As a result, an alternative RF heating technique is now available - mode conversion heating with a high field side launch, discussed in the next section.

At present there is no projected need for current drive capability in order to cancel residual currents driven by neutral-beam injection during unbalanced injection, or to further tailor the equilibrium. However, the available heating techniques lend themselves to current drive, so that if current drive became desirable for any reason only minor modifications to the heating system described here would be needed.

7.4.2 Advantages of HFFW Heating

1) Insensitivity to the magnetic field. The absorption mechanism for fast waves on electrons is Landau damping, which is not dependent on cyclotron resonance effects. 2) Strong damping. NCSX is expected to operate at moderately high susceptibility ($\omega_{pe}^2/\Omega_{ce}^2 \sim 5$), which is a regime intermediate between conventional tokamaks and the spherical torus. High per-pass

damping can be expected for a wide range of operating parameters. 3) Readily available sources and a coupling system which should be insensitive to minor variations in the plasma loading. 350 MHz 1 MW CW klystrons have been developed for particle accelerators. Isolators are available which would allow the klystrons to operate into any load, reducing the risk of source arcs if the plasma edge, and the resultant load seen by the coupler, changes suddenly. 4) The ability to use compact, folded waveguide couplers. 5) If needed, the ability to drive current in a broad profile. 6) No significant heating of the bulk ions. No significant damping on the neutral beam ions, especially if no current drive is desired so that the launched parallel wavenumber can be relatively large (a slow parallel phase velocity inhibits current drive while increasing bulk electron damping).

7.4.3 High Frequency Fast Wave Heating in NCSX

In Figure 7-20 is shown a calculation of the per-pass absorption for HFFW for a model equilibrium with a peak density of 6×10^{19} m^{-3}, a launched $N_{||}$ ($\equiv ck_{||}/\omega$) = 6.8, central magnetic field of 1.2 T, in a hydrogen plasma with a density profile assumed to be $(\text{parabolic})^{0.5}$. A 2% population of fast neutral-beam injected particles is assumed, to check damping on fast ions. Damping is seen to be adequate for central electron temperatures in excess of a few hundred eV.

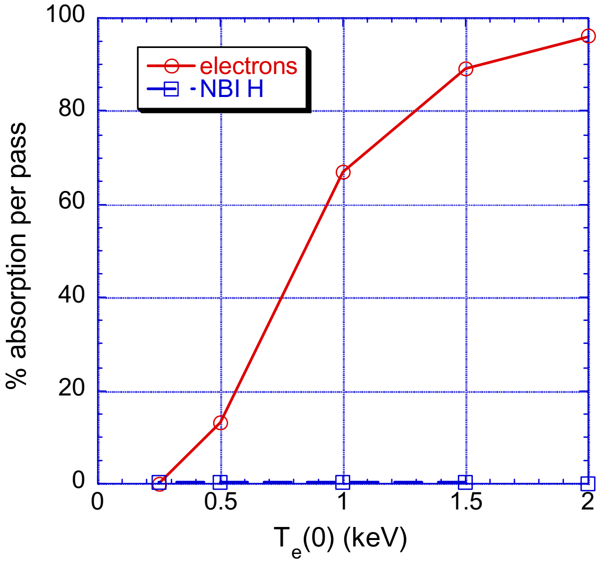

Figure 7-20. Per pass damping as a function of central electron temperature

In Figure 7-21 is shown the computed variation of per-pass damping with central magnetic field. Clearly this heating technique is largely insensitive to the operating field. The primary effect of lowering the field from 2T to 0.8T, for fixed $k_{||}$ at the launcher, is to increase (ω/Ω_{ci}) and therefore increase $k_\perp$. Hence the integrated damping decrement increases slightly, as can be noted in Figure 7-21. In practice, reducing the field would be expected to decrease confinement, so that the target parameters would likely be reduced at lower field. The inverse scaling of $k_\perp$ with magnetic field would maintain strong damping at lowered field.

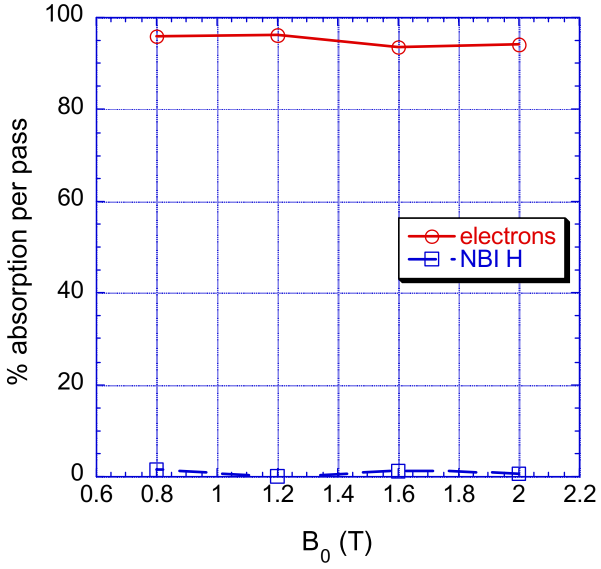

Figure 7-21. Per-pass damping for HFFW as a function of magnetic field

The modeling of HFFW absorption shown in Figures 7-20 and 7-21 was performed with the 1-D integral code METS95, which retains ion damping at high harmonic number.

7.4.4 HFFW Current Drive

Although there is no requirement at present that the HFFW system drive current, modeling has indicated that 6 MW of HFFW has appreciable current drive capability. In Figure 7-22 is displayed the results of a 2D axisymmetric calculation of the current drive efficiency as a function of launched $N_{||}$, using the TORIC code.

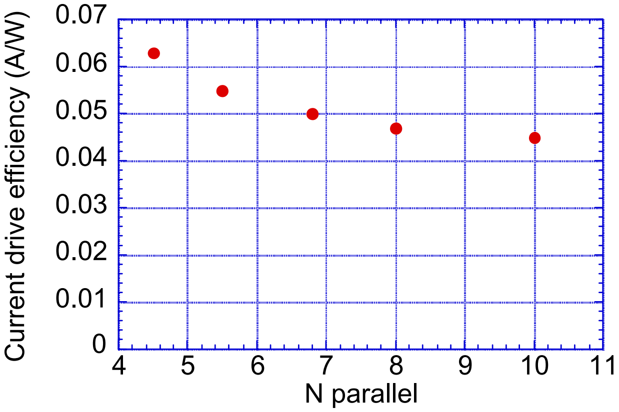

Figure 7-22. Current drive efficiency as a function of $N_{||}$

The highest current drive efficiency is obtained for low $N_{||}$ (or high v_ϕ/v_{Te}). At low $N_{||}$ coupling is primarily to superthermal electrons; hence a decrease in per-pass electron absorption is expected.

This decrease is displayed in Figure 7-23.

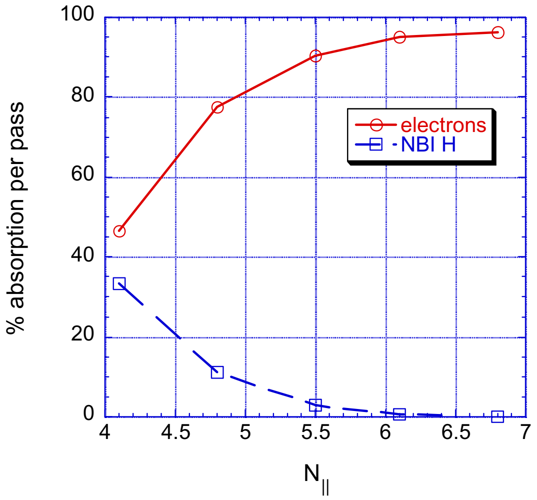

Figure 7-23. Per-pass absorption as a function of $N_{||}$, for 350 MHz HFFW incident on a plasma with $n_e(0)=6 \times 10^{19}$ m^{-3} (parabolic$^{0.5}$), $T_e(0) = T_i(0) = 2$ keV, 2% NBI H. Results from the METS95 code

From Figures 7-22 and 7-23 it is seen that reasonable current drive efficiency can be obtained with a launched $N_{||}$ which is strongly absorbed in a single pass. Therefore the 6 MW HFFW system should be capable of driving ~ 300 kA of noninductive current if needed.

7.4.5 Slow Wave Excitation

A possible concern with the use of fast waves at high frequencies is excitation of the slow or lower hybrid wave in the edge plasma. For 350 MHz the lower hybrid resonance occurs at a density of ~ 5×10^{18} m^{-3}. The right hand fast wave cutoff occurs at a density of ~ 3×10^{18} m^{-3}. In Figure 7-24 is displayed the hot plasma dispersion relation, calculated with the CRF code, for the NCSX model plasma used in conjunction with Figure 7-23. The only slow wave root in evidence is the ion Bernstein wave, which exists between ion cyclotron harmonics and does not couple to the fast wave (lower $k_\perp$) root. The lower hybrid root for these parameters occurs at extremely high $k_\perp$; greater than 10^4 m^{-1}. No coupling from the propagating fast wave to the slow wave would be expected in this case.

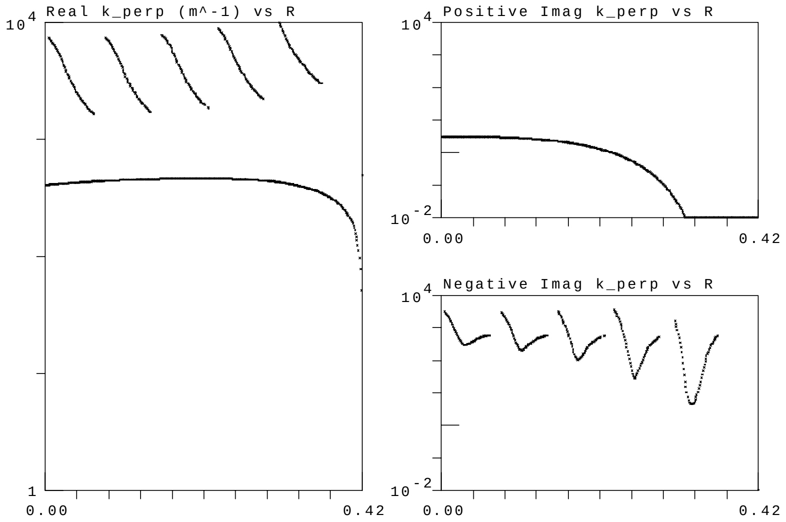

Figure 7-24. Hot plasma dispersion relation for 350 MHz HFFW. The near-vertical roots in the plot of Re($k_\perp$) vs. plasma position denote the ion Bernstein wave roots. The damping decrement for HFFW is given in the positive Im($k_\perp$) plot; the decrement associated with the Bernstein wave is given in the plot of negative Im($k_\perp$). The lower hybrid slow wave root is at $k_\perp > 10^4$ m^{-1}

It should be noted that experiments at 200 MHz in JFT-2M have seen no evidence of coupling to the lower hybrid root.

7.4.6 Launchers

At 350 MHz it is possible to utilize folded waveguide launchers. An example of a dipole folded waveguide launcher designed and built at ORNL as a prototype for installation on the FTU tokamak is shown in Figure 7-25.

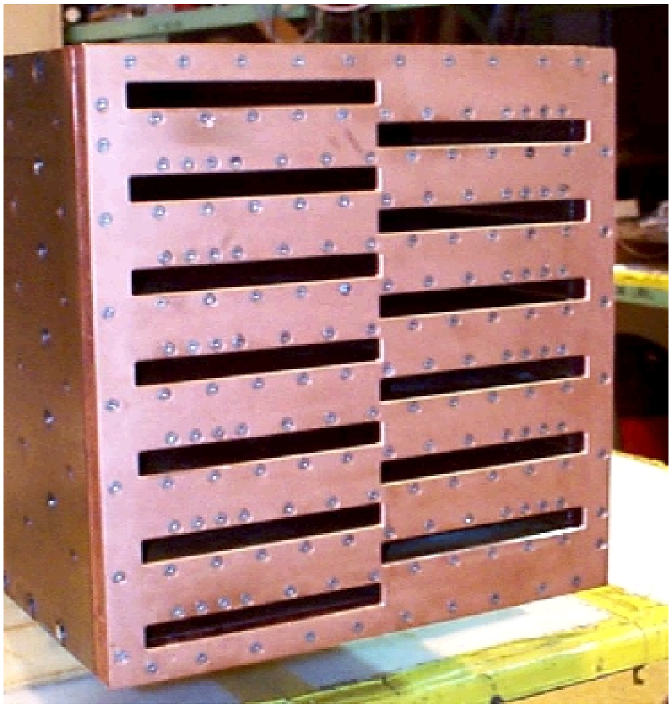

Figure 7-25. 440 MHz folded waveguide launcher, an ORNL prototype designed for FTU

A folded waveguide launcher capable of a directed launch for current drive would be somewhat more complex than a dipole launcher, with at least four apertures in the toroidal direction. Neighboring waveguide apertures would be phased to produce a directed launch of the fast wave.

Six sources (1.2 MW per source, 80% coupled) would be utilized to provide the required 6 MW of coupled power. The baseline design for the 350 MHz coupling system would therefore consist of four folded waveguide couplers, each 24 cm in toroidal extent × 44 cm in poloidal extent. Each coupler would consist of six apertures, each fed by one of the klystron sources through a four-way power splitter. This arrangement permits arbitrary phasing of the six neighboring waveguide apertures in each coupler, so that the launched $N_{||}$ can be varied in real time if necessary by adjusting the relative phase of the klystron sources. The total coupler area would be 0.42 m^2, which implies a power density at the coupler of approximately 14 MW/m^2 at full power. Folded waveguide couplers have demonstrated the capability of operating at high power density during test stand trials at ORNL. However, achieving this power density in NCSX would likely require that the coupler be closely coupled to the fast wave cutoff density, i.e. that the plasma density at the coupler be near 3×10^{18} m^{-3}.

7.5 Mode Conversion RF Heating

7.5.1 Introduction

In ion Bernstein wave mode conversion heating, a fast magnetosonic wave, excited at the boundary of a multiple-ion species plasma, propagates to the ion-ion hybrid layer where it undergoes conversion to the slow wave. Typically, the damping lengths for the slow ion Bernstein wave (IBW) are many times shorter than for the launched fast wave, so that power deposition occurs in a highly localized region near the hybrid layer. When the ion temperature is modest and the species mix is such that mode conversion takes place far from an ion cyclotron resonance, the IBW damps on electrons. For high ion temperatures, or modest concentration of one of the ion species so that the mode conversion layer is located close to a cyclotron resonance, ion damping can be produced.

Mode conversion heating was first successfully demonstrated using a high field side launch in the TFR tokamak[9]. Efficient, localized electron heating using mode conversion was demonstrated in TFTR[10] and more recently has been extensively utilized in C-MOD. In tokamaks, a low field side launch of the fast wave in D-^{3}He has been most commonly employed. Mode conversion with a high field side launch, which is efficient with a wider variety of ion species mixes, has now been utilized successfully in the LHD, WVII-AS, and CHS stellarators. Modeling of NCSX plasmas has indicated that a high field side fast wave launch is necessary to efficiently access the mode conversion surface. Although such a launch would have been exceedingly difficult or impossible to accommodate with the original saddle-coil design for NCSX, it now appears possible that the modular coil design will permit installation of a high field side "combline" antenna. This type of antenna can be constructed with a very small radial build, which lends itself to installation in a shallow "pocket" in the vacum vessel, on the high field side.

The METS 95 code, a 1-D hot plasma full-wave code which has been extensively benchmarked during mode conversion heating experiments in TFTR and C-MOD, has been employed to model mode conversion in NCSX. Mode conversion scenarios for NCSX have now been identified for D-H and D-^{3}He plasmas. Either ion or electron heating can be selected through an appropriate choice of the species mix and launched wavenumber.

7.5.2 Mode Conversion in D-H

The results of modeling D-H mode conversion are shown in Figure 7-26 (a & b). Figure 7-26a is a plot of the dispersion relation for 10% H in a D majority plasma, with a central magnetic field of 2T, a central electron density of 5×10^{19} m^{-3} (parabolic profile), for a fast wave excited at 25 MHz with a wavenumber of 9 m^{-1}. Note that this and all following modeling is largely invariant in (ω/Ω_i); if operation at a lower magnetic field is desired then the launch frequency must be reduced.

For the ion and electron temperatures chosen (T_e=T_i= 1 keV), METS 95 indicates that majority D/minority H mode conversion will produce relatively weak absorption, with a broad deposition profile on the electron population. Since absorption occurs well to the high field side of the hydrogen cyclotron resonance, a relatively high magnetic field is required to obtain core heating - at 20 MHz the magnetic field scales to 1.6T.

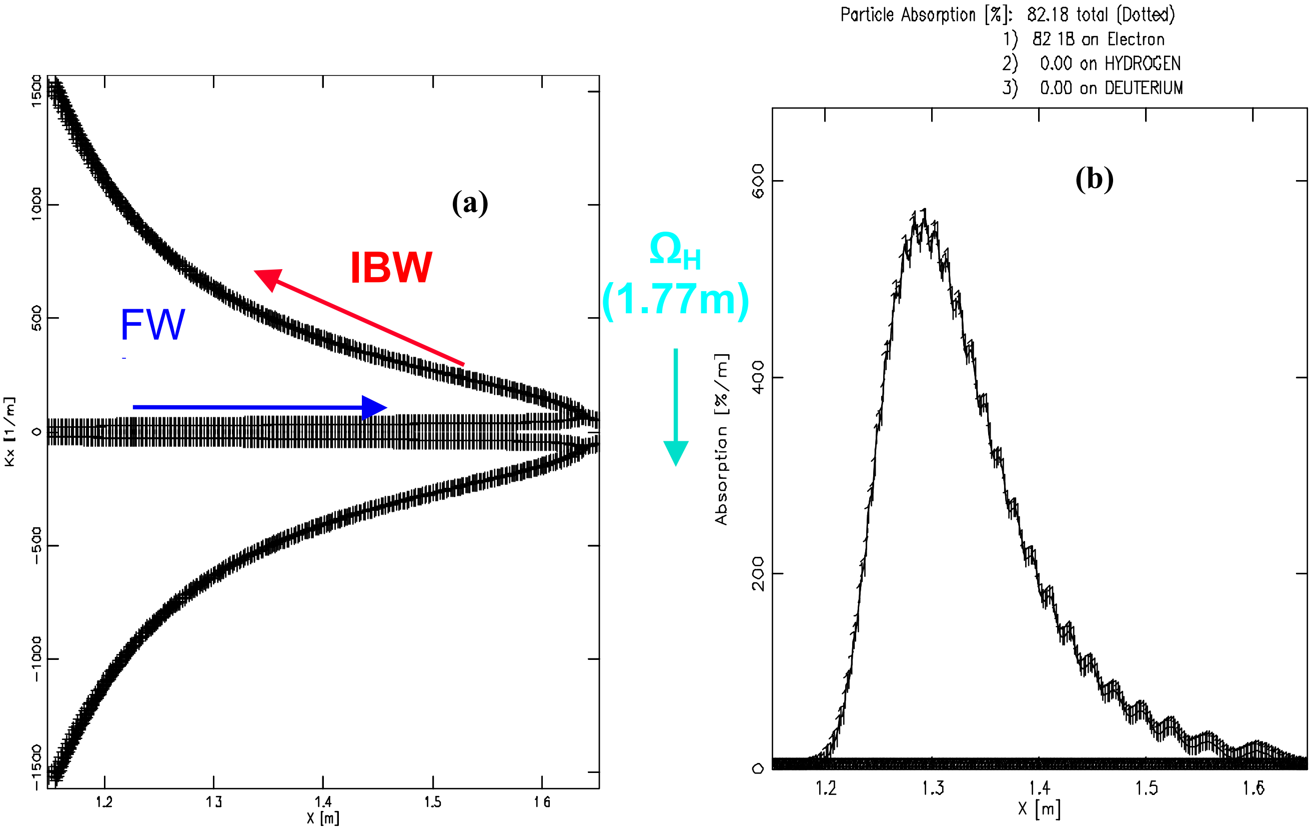

Figure 7-26. Dispersion relation for mode conversion in 10% H/90% D in NCSX (a), and power deposition profile (b). 82% of the launched power is deposited on electrons within the simulation window, with a full-width at half-max of ~15 cm. Central density for the simulation was 5×10^{19} m^{-3} (parabolic profile), central $T_e = T_i = 1$ keV, 2T, with a launched frequency of 25 MHz and wavenumber of 9 m^{-1}

Although the option to use hydrogenic plasmas would permit access to possible low-recycling regimes, operation at the low toroidal field initially available on NCSX with core heating would require a prohibitively low operating frequency (~15 MHz). Finally, lower hydrogen concentrations (~5%) would allow experiments in conventional light ion minority heating, although the fast ion tail population is not expected to be well confined in NCSX.

7.5.3 Mode Conversion in H-^{3}He

The most promising and flexible ion system for mode conversion heating in NCSX H-^{3}He, which should permit localized ion or electron heating (or electron current drive), either on or off axis. With a transmitter frequency of 20 MHz (the lowest practical frequency for the existing PPPL sources), on axis heating can be obtained at central magnetic fields as low as 1.3T.

Localized electron heating can be produced in H-^{3}He for a wide range of species mixes and wavenumbers. However, ion heating is predicted for low concentrations of either hydrogen (light ion minority) or helium (heavy ion minority). In Figure 7-17 (a & b) the dispersion relation and deposition profile for 10%H in ^{3}He are shown. Deposition is predicted to be primarily on the hydrogen population. In order to produce ion heating it is necessary to launch the 25 MHz fast wave at high wavenumber (12 m^{-1}) in order to obtain Doppler-broadened Bernstein wave damping on the hydrogen..

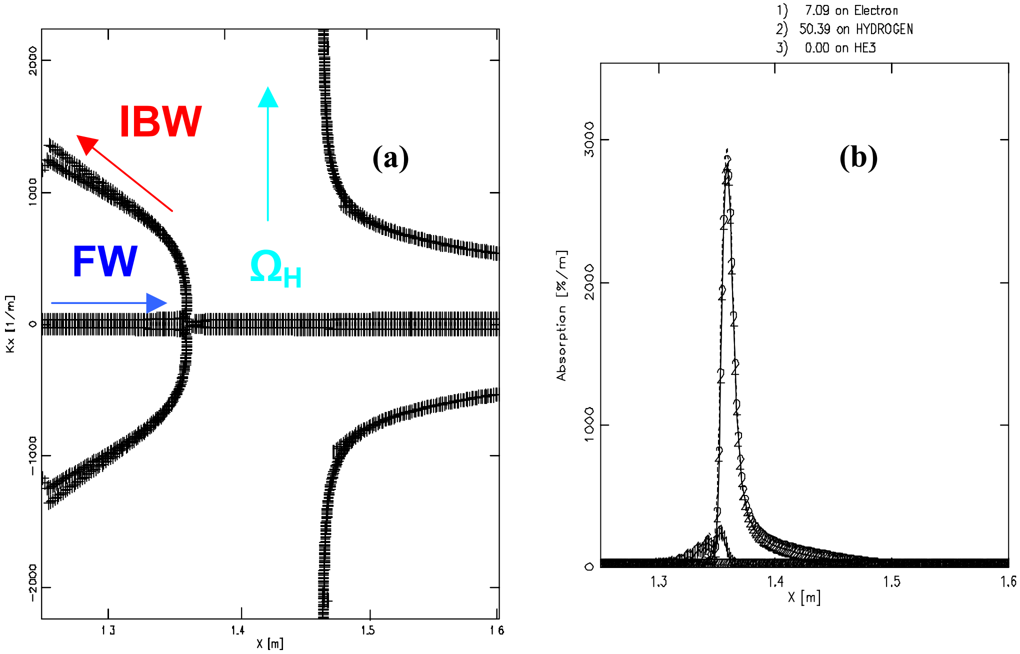

Figure 7-27 (a & b). Dispersion relation for mode conversion in 10% H, 90% ^{3}He plasmas. Excited frequency is 25 MHz at a wavenumber of 12 m^{-1}, with a central magnetic field of 1.6T, central density of 5 × 10^{19} m^{-3} (parabolic profile), central $T_e = T_i$ = 1 keV. 57% of the incident power is coupled to the hydrogen population via Doppler broadened cyclotron absorption

Ion tail formation under these conditions will be lessened due to the high hydrogen concentration. If a lower launched wavenumber or a higher hydrogen concentration is chosen, then localized electron heating rather than ion heating is predicted. The case modeled here corresponds to operation at 1.3T if the frequency is lowered to 20 MHz. Note that the deposition profile is extremely narrow, with a FWHM of approximately 2 cm. 3D effects will likely broaden the deposition profile, but insofar as the mod-B surfaces are also flux surfaces it is likely that very narrow power deposition profiles can be obtained.

At higher toroidal fields ion heating can be produced with a reduced ^{3}He fraction. In Figure 7-28 (a & b) is shown the dispersion relation and power deposition profile for 10% ^{3}He in a hydrogen minority, for 25 MHz operation at 2.2T.

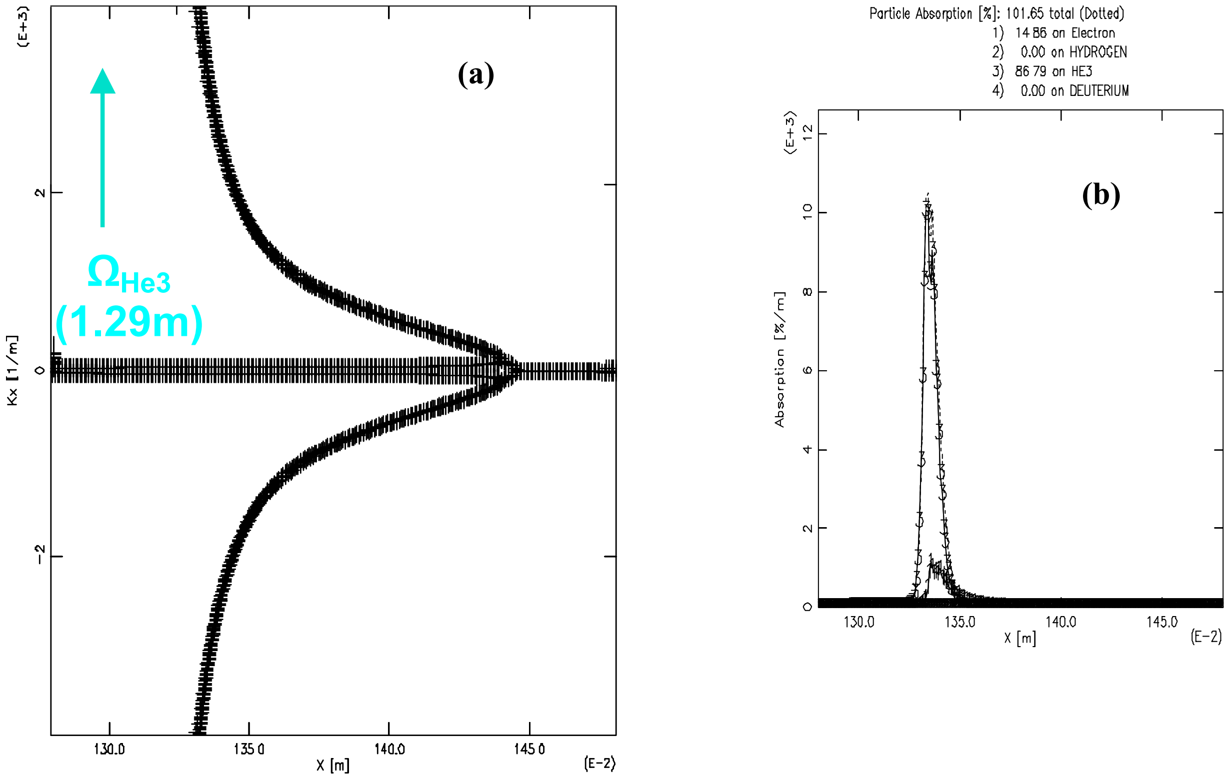

Figure 7-28 (a &b) Dispersion relation and power deposition profile for mode conversion in 10% ^{3}He, 90% H at 2.2T, 25 MHz, launched wavenumber of 6 m^{-1}, central density of 1×10^{20} m^{-3}, 1.0 keV ion and electron temperatures

In this example the magnetic field scales to 1.76T for 20 MHz operation. However, if deposition at the 2/3 radius is desired, then the field scales to 1.5T. Deposition at large minor radius may be acceptable here, since this case corresponds to IBW ion damping near a cyclotron resonance, which is desirable for rf shear flow generation. Note that the deposition layer (at least in this 1-D model) is extremely narrow, with a FWHM of about 1 cm.

For species mixes intermediate to the cases shown in Figures 7-27 and 7-28 (i.e. more nearly equal concentrations of H and ^{3}He), electron damping with a very narrow deposition profile is predicted. This can provide a localized heating source for measurements of the electron thermal diffusivity, or a localized current drive source for modification of the iota profile. Note that with two antennas iota profile modification can be accomplished with a minimal net current drive, by injecting both co- and counter- current.

These capabilities (localized or broad electron heating, localized current drive or current profile control, localized ion heating,, possible rf shear flow drive) combine to make mode conversion heating an attractive physics tool for NCSX.

7.5.4 RF Systems and Antennas for Mode Conversion

As stated earlier, the most attractive antenna for a high field side launch in NCSX is probably the combline, which utilizes "passive" excitation of a wide array of current straps. The combline was pioneered at GA[11] and has been tested on JFT-2M and to some extent on DIII-D. In order to provide the required 6 MW of RF heating, three antennas would be installed in NCSX, on the high field side of the device, with each antenna centered about the "bullet" plasma cross section.

The existing PPPL FMIT units could be used for mode conversion in NCSX, in a time-sharing arrangement with NSTX. An engineering study has determined that operation of two of the four FMIT sources over the frequency range of 20 - 30 MHz is feasible; this would provide 4 MW of rf source power. An additional 3-4 MW would be available from the remaining two sources, depending on the degree to which they were reconfigured. Although the sharing of sources precludes simultaneous RF heating of NSTX and NCSX, the transmitter modifications proposed would require minimal down time to change frequencies. A changeover from the NSTX operating frequency of 30 MHz to one of the NCSX operating frequencies (or the reverse) is expected to take a few days.

References

[1] A.H. Boozer, Phys. Fluids **24** (1981) 1999.
[2] D.A. Spong, J. Carlsson, D.B. Batchelor, et al., Bull. Am. Phys. Soc. **44** (1999) 215.
[3] R.V. Budny, D.C. McCune, M.H. Redi, J. Schivell, R.M. Wieland, Phys. Plasmas **3** (1996) 4583.
[4] S.P. Hirshman, J.C. Whitson, Phys. Fluids **26** (1983) 3553.
[5] A.H. Boozer, G. Kuo-Petravic, Phys. Fluids **24** (1981) 851.

[6] S.P. Hirshman, D.J. Sigmar, Phys. Fluids **19** (1976) 1532.
[7] A.C. Hindmarsh, "Odepack, a Systematized Collection of ODE Solvers, in Scientific Computing," R.S. Stepleman et al. (Eds.), North-Holland, Amsterdam, 1983, pp. 55-64.
[8] M. Zarnstorff, 2000 IAEA Fusion Energy Meeting, Sorrento, Italy (Oct. 2000).
[9] Equippe TFR, in Plasma Physics and Controlled Nuclear Fusion Research, Proc. 9th International Conf., Baltimore, 1982, Vol. 2, p. 17.
[10] R. Majeski et al., Phys. Rev. Lett. **76** (1996) 764.
[11] C. P. Moeller et al., in Radio Frequency Power in Plasmas, Proc. 10th Top. Conf., Boston, 1993 (AIP Conf. Proc. Vol. 289), p. 323.